

Chapter 9

Role of Computational Modeling for Dose Determination



Ricardo Salvador, Dennis Q. Truong, Marom Bikson, Alexander Opitz, Jacek Dmochowski, and Pedro C. Miranda

Computational Forward Models in Transcranial Direct Current Stimulation

Introduction to Dose Definition and Selection

Dose, as defined in the context of transcranial stimulation with magnetic or electrical fields (E-fields), includes all the controllable parameters of the stimulation device that affect the electromagnetic field induced in the body (Peterchev et al. 2012). In the case of tDCS, this includes parameters such as the size, geometry, position, orientation and number of electrodes, the current intensity and polarity in each electrode, the duration of the applied current and the duration of the ramp-up/down period. Other parameters related to the experimental protocol and the skin preparation techniques

R. Salvador
Neuroelectrics, Barcelona, Spain

D. Q. Truong
Department of Biomedical Engineering, The City College of the City University of New York, New York, NY, USA

M. Bikson
Department of Biomedical Engineering, The City College of New York, New York, NY, USA

A. Opitz
Department of Biomedical Engineering, University of Minnesota, Minneapolis, MN, USA

J. Dmochowski
Neural Engineering Laboratory, Department of Biomedical Engineering, Grove School of Engineering, The City College of the City University of New York, New York, NY, USA

P. C. Miranda (✉)
Instituto de Biofísica e Engenharia Biomédica, Faculdade de Ciências, Universidade de Lisboa, Lisbon, Portugal
e-mail: pcmiranda@fc.ul.pt

used can also be included in this definition of dose to the extent they influence electromagnetic fields in the body – though they are always important in the broader content of protocol reproducibility. Replicating all of these dose parameters across subjects does not guarantee, however, that the subjects' response will be the same. This has become increasingly evident by studies indicating that the responses to tDCS can vary substantially across subjects within the same protocol (Lopez-Alonso et al. 2014; Wiethoff et al. 2014). One cause for this difference is the fact that the E-field distribution in the head during tDCS can be substantially different across subjects due to individual differences in head geometry. Since direct *in vivo* measurement of the E-field distribution during tDCS is not possible, except in special cases where implanted electrodes are present (Datta et al. 2016; Dymond et al. 1975; Opitz et al. 2016), computational models remain the only practical tool available to predict E-field in the brain for a given tDCS dose. Information from these models can be used to adjust dose parameters to induce comparable E-field across subjects, or it can be used to optimize these parameters to maximize the effects in a specific target cortical region (Dmochowski et al. 2011; Ruffini et al. 2014).

Methods for Generation of Computational Models

The first models to predict the E-field in brain stimulation techniques relied on analytical solutions of the underlying physical equations (Eaton 1992; Rush and Driscoll 1968). The complexity of such approaches often demanded drastic simplifications at the level of head geometry, number of tissues involved and electrode/coil geometry. Numerical computational approaches were soon identified as promising alternatives, but the limited computational resources available at first imposed similar limitations to the models (Roth et al. 1991; Tofts 1990). As such, many of the first computational studies of E-field distribution induced in tDCS adopted spherical head models (Miranda et al. 2006) or computer-aided design (CAD) generated simplified geometries (Wagner et al. 2007). The advent of powerful computational resources has made it possible to build increasingly realistic head and electrode models (Datta et al. 2009a; Oostendorp et al. 2008).

Table 9.1 summarizes several published studies that have employed computational models of tDCS. Most of the recent studies have used realistic head models, and they employ similar techniques to generate such models. A generalized pipeline to create computational models is shown in Fig. 9.1. It should be mentioned that although the studies usually employ the same steps as those highlighted in the figure, the methods employed at each step can be substantially different across studies. The description of the studies presented in Table 9.1 shows the wide variety of electrode configurations and geometries that has been studied (see columns 'Electrodes' and 'Montages'). It also shows that the studies can be used in a variety of applications, such as investigating the fundamental properties of the induced E-field, studying the distribution of the E-field in montages typically used in clinical settings, optimizing montages to target specific cortical areas and/or studying the

Table 9.1 List of all studies involving computational models in tDCS

Reference	Tissues represented	Electrodes	Montages	Study description / Additional comments
Spherical head models				
1. Miranda et al. (2006)	$\sigma_{Scalp} = 0.45 \text{ S/m}$ $\sigma_{Skull} = 0.006 \text{ S/m}$ $\sigma_{Brain} = 0.45 \text{ S/m}$ Isotropic.	Rectangular: $5 \times 5 \text{ cm}^2$ $6.5 \times 15 \text{ cm}^2$. Homogeneous conductivity: 2 S/m.	4 electrode montages.	Type (1).
2. Datta et al. (2008)	$\sigma_{Scalp} = 0.465 \text{ S/m}$ $\sigma_{Skull} = 0.01 \text{ S/m}$ $\sigma_{CSF} = 1.65 \text{ S/m}$ $\sigma_{Brain} = 0.2 \text{ S/m}$ Isotropic.	Cylindrical 0.5 cm^2 . Ring (variable diameters) Homogeneous conductivity: $5.9 \times 10^7 \text{ S/m}$.	6 electrode montages.	Type (1) and (2). Concentric ring electrodes induced a field with the highest focality and directionality.
3. Faria et al. (2011)	$\sigma_{Scalp} = 0.465 \text{ S/m}$ $\sigma_{Skull} = 0.0083 \text{ S/m}$ $\sigma_{CSF} = 1.79 \text{ S/m}$ $\sigma_{Brain} = 0.332 \text{ S/m}$ Isotropic.	Cylindrical with areas between $1 - 35 \text{ cm}^2$. Homogeneous conductivity: 0.332 S/m.	Various bipolar configurations.	Type (1).
4. Rampersad et al. (2012)	$\sigma_{Scalp} = 0.435 \text{ S/m}$ $\sigma_{Brain} = 0.333 \text{ S/m}$ Isotropic. The skull was given several different properties: Isotropic, three-layers, anisotropic.	Rectangular: 35 cm^2 . Homogeneous conductivity: 1.4 S/m.	Several bipolar configurations with electrodes separated by 180° , 90° and 45° .	Type (1). Single layer anisotropic skull or a single layer isotropic skull with a conductivity equal to that of the conductivity in the radial direction of the anisotropic model, gives similar results to 3-layered model.
CAD generated models				
5. Wagner et al. (2007)	$\sigma_{Scalp} = 0.465 \text{ S/m}$ $\sigma_{Skull} = 0.01 \text{ S/m}$ $\sigma_{CSF} = 1.654 \text{ S/m}$ $\sigma_{GM} = 0.276 \text{ S/m}$ $\sigma_{WM} = 0.126 \text{ S/m}$ Isotropic.	Rectangular: $5 \times 5 \text{ cm}^2$ $7 \times 5 \text{ cm}^2$ $1 \times 1 \text{ cm}^2$ $7 \times 7 \text{ cm}^2$.	7 bipolar montages.	Type (1), (3) and (4). Implemented 3 stroke models.
Models generated from segmentation of MR images				
6. Oostendorp et al. (2008)	$\sigma_{Scalp} = 0.33 \text{ S/m}$ $\sigma_{Skull} = 0.102 \text{ S/m}$ $\sigma_{CSF} = 1.79 \text{ S/m}$ $\sigma_{GM} = 0.33 \text{ S/m}$ $\sigma_{WM} = 0.14 \text{ S/m}$ Isotropic. For WM and skull, anisotropy was also included.	Rectangular: $5 \times 9 \text{ cm}^2$ (patch projected into scalp).	Anode over LM1 and cathode over RSO.	Type (1).

(continued)

Table 9.1 (continued)

Reference	Tissues represented	Electrodes	Montages	Study description / Additional comments
7. Datta et al. (2009a)	$\sigma_{Scalp} = 0.465 \text{ S/m}$ $\sigma_{Skull} = 0.01 \text{ S/m}$ $\sigma_{CSF} = 1.65 \text{ S/m}$ $\sigma_{GM} = 0.2 \text{ S/m}$ $\sigma_{WM} = 0.2 \text{ S/m}$ Isotropic.	Rectangular: $5 \times 7 \text{ cm}^2$. Cylindrical 0.5 cm^2 . Modelled with a copper layer ($5.9 \times 10^7 \text{ S/m}$) on top of a layer of gel (0.3 S/m).	Rectangular anode over LMI and cathode over RSO. 4 × 1 cylindrical electrode configuration (1 anode over LMI and 4 cathodes surrounding it).	Type (1), (2) and (3).
8. Datta et al. (2009b)	Same as (7).			Type (1). No significant temperature increases were reported in any tissue including the scalp during tDCS.
9. Sadleir et al. (2010)	$\sigma_{Scalp} = 0.43 \text{ S/m}$ $\sigma_{Skull} = 0.0015 \text{ S/m}$ $\sigma_{CSF} = 1.8 \text{ S/m}$ $\sigma_{GM} = 0.1 \text{ S/m}$ Isotropic. σ_{WM} : Anisotropic Other tissues were included (total of 11).	Rectangular: 22 cm^2 . Homogeneous conductivity: 1 S/m.	Anode over F3 and cathode over RSO. Anode over F4 and cathode over LSO.	Type (1) and (2).
10. Datta et al. (2010)	Same as (7). Skull holes were modelled (either filled with CSF or scar tissue).	Rectangular: $5 \times 7 \text{ cm}^2$. Modelled as in (7).	Anode over C3 and cathode over RSO. Anode over O1 and cathode over RSO.	Type (1) and (4). Placing electrode over skull hole significantly affects the E-field distribution, but if the hole is midway between the two electrodes, no significant effects occur.
11. Parazzini et al. (2011)	$\sigma_{Scalp} = 0.012147 \text{ S/m}$ $\sigma_{Skull} = 0.020028 \text{ S/m}$ $\sigma_{CSF} = 2 \text{ S/m}$ $\sigma_{GM} = 0.027512 \text{ S/m}$ $\sigma_{WM} = 0.027656 \text{ S/m}$ Isotropic. Many other tissues were considered (total of 26).	Rectangular: Anode: $3.5 - 35 \text{ cm}^2$ Cathode: $25 - 100 \text{ cm}^2$ Electrodes modelled as perfect conductors.	Anode over C3 and cathode over Fp2.	Type (1), (2) and (3).

Table 9.1 (continued)

Reference	Tissues represented	Electrodes	Montages	Study description / Additional comments
12. Mendonca et al. (2011)	$\sigma_{Scalp} = 0.465 S/m$ $\sigma_{Skull} = 0.01 S/m$ $\sigma_{CSF} = 1.65 S/m$ $\sigma_{GM} = 0.276 S/m$ $\sigma_{WM} = 0.126 S/m$ Isotropic. Many other tissues were considered (total of 8). A synthetic neck and shoulder region was added with an isotropic conductivity of 0.17 S/m.	Rectangular: $4 \times 4 cm^2$ and $8 \times 10 cm^2$. Modelled as in (7).	Anode over C3 and the cathode over cervical/thoracic transition dorsal midline. Anode over RSO and cathode unchanged. Anode over C3 and cathode over RSO.	Type (1), (3) and (5). Effects of extracephalic return electrodes and application to fibromyalgia.
13. Halko et al. (2011)	Same as (12) (without “synthetic” neck-shoulder region). Includes a stroke lesion modelled as CSF.	Rectangular: $5 \times 7 cm^2$. Modelled as in (7).	Anode over Cz and the cathode over Oz.	Type (4) and (5). Patient specific model of a patient with a stroke lesion.
14. Datta et al. (2011)	Same as (12) but with synthetic neck-shoulder region with a conductivity of 0.35 S/m. Includes a stroke lesion modelled as CSF.	Rectangular: $5 \times 5 cm^2$. Modelled as in (7).	Anode over C3 and cathode over: (a) Right shoulder (b) Right mastoid (c) Right orbitofrontal Anode over C4 and cathode over left shoulder	Type (4) and (5). Position of return electrode significantly affected E-field distribution.
15. Dmochowski et al. (2011)	Same as (7) but with muscle and air cavities segmented as well.	Cylindrical $1.1 cm^2$. Modelled as in (7).	64 possible positions according to the 10/10 international system.	Type (6). Algorithms to determine current intensity and polarity in pre-defined grid of electrodes to optimize E-field in target region.
16. Suh et al. (2012)	$\sigma_{Scalp} = 0.33 S/m$ $\sigma_{Skull} = 0.0132 S/m$ $\sigma_{CSF} = 1.79 S/m$ $\sigma_{GM} = 0.33 S/m$ $\sigma_{WM} = 0.14 S/m$ Isotropic. Skull and WM anisotropy was also modelled.	Cylindrical $0.5 cm^2$. Modelled as homogeneous.	Anode over C3 and cathode over C4.	Type (1). Skull anisotropy significantly affects the E-field distribution whereas the WM anisotropy has a smaller effect (except on deeper regions).
17. Dasilva et al. (2012)	Same as (12), but more tissues were segmented (total of 15).	Rectangular: $5 \times 7 cm^2$ Modelled as in (7).	Anode over C3 and cathode over RSO.	Type (3) and (5). Application to chronic migraine.
18. Turkeltaub et al. (2012)	Same as (12).	Rectangular: $5 \times 5 cm^2$. Modelled as in (7).	Anode over RpTC (midway between T7 and TP7) and cathode placed over LpTC (midway between T8 and TP8).	Type (3) and (5). Application to dyslexia study.

(continued)

Table 9.1 (continued)

Reference	Tissues represented	Electrodes	Montages	Study description / Additional comments
19. Datta et al. (2012)	Same as (12) (without “synthetic” neck-shoulder region).	Rectangular: $5 \times 7 \text{ cm}^2$. Cylindrical 1.1 cm^2 . Modelled as in (7).	Same as (7).	Type (1) and (3). Compares E-field distribution across 3 different subjects. Reports the need to incorporate subject specific models.
20. Minhas et al. (2012)	Same as (19).			Type (1) and (4). Compares E-field distribution in an adult model and a model of a child (12 years old).
21. Sadleir et al. (2012)	Same as (9).		19 possible locations selected from the 10 to 20 system.	Type (6). Algorithms to determine current intensity and polarity in pre-defined grid of electrodes to optimize E-field’s magnitude in target region.
22. Parazzini et al. (2012)	Same as (11).	Rectangular: $5 \times 7 \text{ cm}^2$. Modelled as perfect conductors.	1 electrode over LTA (halfway between C3 and T5) and another one over Fp2. Electrodes over F3 and F4.	Type (3) and (6). Study of electrode montages used in the treatment of tinnitus.
23. Truong et al. (2013)	Same as (19). Includes fat as a separate tissue.	Same as (19).	Same as in (7) Anode over F8 and cathode over LSO.	Type (1), (3) and (4). Compares E-field distribution in individualized models of 5 subjects with various body-mass indexes (ranging from normal to obese).
24. Shahid et al. (2013)	$\sigma_{Scalp} = 0.43 \text{ S/m}$ $\sigma_{Skull} = 0.015 \text{ S/m}$ $\sigma_{CSF} = 1.79 \text{ S/m}$ $\sigma_{GM} = 0.32 \text{ S/m}$ $\sigma_{WM} = 0.15 \text{ S/m}$ Isotropic. WM anisotropy was also modelled. Other tissues were also segmented (total of 15).	Rectangular: $5 \times 5 \text{ cm}^2$. Homogeneous conductivity: 1.4 S/m .	Anode over C3 and cathode over Fp2.	Type (1) and (3). Reports significant effects of anisotropy in current density distribution.

Table 9.1 (continued)

Reference	Tissues represented	Electrodes	Montages	Study description / Additional comments
25. Miranda et al. (2013)	$\sigma_{Scalp} = 0.33 S/m$ $\sigma_{Skull} = 0.008 S/m$ $\sigma_{CSF} = 1.79 S/m$ $\sigma_{GM} = 0.32 S/m$ $\sigma_{WM} = 0.15 S/m$ Isotropic.	Rectangular $5 \times 7 cm^2$, $3 \times 3 cm^2$. Cylindrical πcm^2 . Homogeneous conductivity: 2 S/m.	Anode over C3 and cathode over right SO. The rectangular anodes were rotated 45° so that their edge is approximately parallel to the central sulcus.	Type (1) and (3). Reports E-field maxima at the bottom of the sulci under the electrodes.
26. Dmochowski et al. (2013)	Same as (12) (without “synthetic” neck-shoulder region). Includes stroke lesions modelled as CSF.	Cylindrical $1.1 cm^2$. Modelled as in (7).	74 possible positions according to the 10/10 international system.	Type (4) and (6). “Optimized” electrode positions increased E-field strength, as compared to conventional montages, at stroke lesion sites in 8 patients.
27. Kessler et al. (2013)	Same as (19).	Rectangular: $25 cm^2$. Cylindrical $0.95 cm^2$. Modelled as in (7).	Rectangular electrodes: Anode/cathode over C3/C4. Anode/cathode over the posterior left/right STG. Anode/cathode over F3/F4. Anode cathode over left M1/RSO 4×1 cylindrical electrode configuration (1 anode over LM1 and 4 cathodes surrounding it). Two distances from cathodes to anode were modelled	Type (1), (3) and (4). 4 models of healthy adults and 2 models of children (ages 8 and 12) were created. For the same currents, the E-field in the children models is stronger.

(continued)

Table 9.1 (continued)

Reference	Tissues represented	Electrodes	Montages	Study description / Additional comments
28. Parazzini et al. (2013a)	Same as (11).	Anodes: Rectangular $5 \times 7.5 \text{ cm}^2$ copper conductor ($5.9 \times 10^7 \text{ S/m}$) on top of a $7 \times 8 \text{ cm}^2$. “Sponge” (0.3 S/m). Cathode: Same as before but with different dimensions for the copper $5 \times 9.5 \text{ cm}^2$ and sponge $7 \times 10 \text{ cm}^2$.	Anode over Fz and cathode over the right tibia. Anode over T3 and cathode over right deltoid. Two anodes over C3 and C4 and a cathode over right deltoid.	Type (1) and (3). Reports current density magnitude in the midbrain, pons and medulla. Data suggests that interference of the extracephalic reference electrodes with the brainstem should be limited.
29. Parazzini et al. (2013b)	Same as (11).		Anode/cathode over F3/F4. Same as the last two configurations in (28).	Type (1) and (3). Reports current density magnitude in the heart. The induced current density in the heart is lower than reported values for ventricular fibrillation threshold.
30. Wagner et al. (2014a, b)	$\sigma_{\text{Scalp}} = 0.43 \text{ S/m}$ $\sigma_{\text{Skull Compacta}} = 0.007 \text{ S/m}$ $\sigma_{\text{Skull Spongiosa}} = 0.025 \text{ S/m}$ $\sigma_{\text{CSF}} = 1.79 \text{ S/m}$ $\sigma_{\text{GM}} = 0.33 \text{ S/m}$ $\sigma_{\text{WM}} = 0.14 \text{ S/m}$ Isotropic. WM was also modelled as anisotropic.	Rectangular $5 \times 7 \text{ cm}^2$. Homogeneous conductivity: 1.4 S/m .	Anode over left M1 and cathode over RSO. Anode and cathode place bilaterally over the area of TP9/10, P7/8, T7/8 and CP5/6.	Type (1) and (3). Reports moderate changes due to WM anisotropy in current density direction in GM. In the WM bigger differences are observed.
31. Rampersad et al. (2014)	$\sigma_{\text{Scalp}} = 0.465 \text{ S/m}$ $\sigma_{\text{Skull Compacta}} = 0.007 \text{ S/m}$ $\sigma_{\text{Skull Spongiosa}} = 0.025 \text{ S/m}$ $\sigma_{\text{CSF}} = 1.65 \text{ S/m}$ Isotropic. GM/WM, cerebellar GM/WM and brainstem: Anisotropic with volume normalized approach. Other tissues were considered (total of 9).	Rectangular $5 \times 7 \text{ cm}^2$. Homogeneous conductivity: 1.4 S/m .	Anode-cathode: LM1-RSO LDLPFC-RSO LDLPFC-RDLPFC LIFG-RSO Oz-Cz Right cerebellum – right cheek.	Type (1) and (3). Reports sub-optimal field strengths in the target regions for each electrode configuration.

Table 9.1 (continued)

Reference	Tissues represented	Electrodes	Montages	Study description / Additional comments
32. Shahid et al. (2014)	Same as (24). WM, GM and skull anisotropy was included as well. Other tissues were also represented (total of 19).	Rectangular: $5 \times 5 \text{ cm}^2$. Homogeneous conductivity: 1.4 S/m. Cylindrical 1.1 cm^2 . Modelled as in (7).	Rectangular anode over C3 and cathode over Fp2. Cylindrical anode over C3 and cathodes over C1, FC3, CP3 and C5. Cylindrical anode over C1 and cathodes over Cz, C3, FC1 and CP1.	Type (1) and (3). The effects of anisotropy would not affect the clinical decision in the examples analyzed. However, they are of importance if cellular model predictions are to be made.
33. Ruffini et al. (2014)	Same as (25).	Cylindrical $\pi \text{ cm}^2$, 25 cm^2 . Homogeneous conductivity: 2 S/m.	π electrodes: Any one of 27 positions in the 10–20 system. 25 cm^2 electrodes: Several bipolar montages based on literature.	Type (3) and type (6).
34. Parazzini et al. (2014a)	Same as (11) but with skin conductivity set to 0.1 S/m.	Rectangular $5 \times 7 \text{ cm}^2$ copper conductor ($5.9 \times 10^7 \text{ S/m}$) on top of sponge (1.4 S/m).	Cathode over the midpoint between C3 and F3 and anode over: RSO area; Right shoulder area.	Type (3) and (4). Determines the E-field distribution in children models. The cathode was placed in the most common epileptogenic focus in children.
35. Parazzini et al. (2014b)	Same as (11).	Rectangular $5 \times 7 \text{ cm}^2$ copper conductor ($5.9 \times 10^7 \text{ S/m}$) on top of $7 \times 8 \text{ cm}^2$ sponge (0.3 S/m).	Anode/cathode centered over cerebellum and reference electrode over the right arm.	Type (3). Reports current density distribution in tDCS of the cerebellum.
36. Gillick et al. (2014)	No details provided.	Rectangular $5 \times 7 \text{ cm}^2$. No details provided regarding modelling.	Anode/cathode over C3/C4. Anode/cathode over LM1/RSO.	Type (3) and (5). Shows results of E-field modelling in a child brain model with a stroke.

(continued)

Table 9.1 (continued)

Reference	Tissues represented	Electrodes	Montages	Study description / Additional comments
37. Brunoni et al. (2014)	Same as (12) (without “synthetic” neck-shoulder region).	Rectangular: $5 \times 7 \text{ cm}^2$. Modelled as in (7).	Anode over left DLPFC and cathode either over occipital area or left TPJ.	Type (3). Shows E-field distribution in montages typically used in schizophrenia.
38. Metwally et al. (2015)	$\sigma_{Scalp} = 0.33 \text{ S/m}$ $\sigma_{Skull} = 0.0132 \text{ S/m}$ $\sigma_{CSF} = 1.79 \text{ S/m}$ $\sigma_{GM} = 0.33 \text{ S/m}$ $\sigma_{WM} = 0.14 \text{ S/m}$ Isotropic. WM and skull were also modelled as anisotropic.	Rectangular: $5 \times 7 \text{ cm}^2$. Cylindrical 0.5 cm^2 . Homogeneous conductivity: $5.8 \times 10^7 \text{ S/m}$.	Rectangular anode over C3 and cathode over RSO. 4×1 cylindrical electrode configuration (1 anode over LM1 and 4 cathodes surrounding it). Cylindrical anode over C3 and cathode over C4.	Type (1) and (3). The presence of WM anisotropy leads to significant differences in the E-field direction, especially within the sulci.
39. Opitz et al. (2015)	$\sigma_{Scalp} = 0.25 \text{ S/m}$ $\sigma_{Skull \text{ Compacta}} = 0.008 \text{ S/m}$ $\sigma_{Skull \text{ Spongiosa}} = 0.025 \text{ S/m}$ $\sigma_{CSF} = 1.79 \text{ S/m}$ Isotropic. The GM and WM were considered anisotropic. Other tissues were considered (total of 8 tissues).	Rectangular: $5 \times 7 \text{ cm}^2$. Homogeneous conductivity: 1.79 S/m , but other values were considered as well.	Same as (25).	Type (1) and (3). Studies the influence of several parameters such as skull thickness, sulcal depth and CSF thickness on E-field distribution.
40. Saturnino et al. (2015)	$\sigma_{Scalp} = 0.25 \text{ S/m}$ $\sigma_{Skull \text{ Compacta}} = 0.008 \text{ S/m}$ $\sigma_{Skull \text{ Spongiosa}} = 0.025 \text{ S/m}$ $\sigma_{CSF} = 1.654 \text{ S/m}$ $\sigma_{GM} = 0.275 \text{ S/m}$ $\sigma_{WM} = 0.126 \text{ S/m}$ Isotropic. Other tissues were considered (total of 8 tissues).	Rectangular: $5 \times 7 \text{ cm}^2$. Ring: Outer/inner diameters: $5 \text{ cm} / 2.5 \text{ cm}$. Cylindrical 1.1 cm^2 or $\pi \text{ cm}^2$. Electrodes modelled with increasing degrees of complexity.	Rectangular/ring anode over C3 and cathode over RSO. $4 + 1$ cylindrical electrode configuration (1 anode over C3 and 4 cathodes surrounding it).	Type (1) and (3). The way the electrodes are modelled can significantly affect the E-field distribution. Important parameters include the location of the metal connector and the conductive rubber’s conductivity.

Table 9.1 (continued)

Reference	Tissues represented	Electrodes	Montages	Study description / Additional comments
41. Laakso et al. (2015)	$\sigma_{Scalp} = 0.08 \text{ S/m}$ $\sigma_{Skull\ Compacta} = 0.013 \text{ S/m}$ $\sigma_{Skull\ Spongiosa} = 0.06 \text{ S/m}$ $\sigma_{CSF} = 1.8 \text{ S/m}$ $\sigma_{GM} = 0.1 \text{ S/m}$ $\sigma_{WM} = 0.1 \text{ S/m}$ Isotropic. Other tissues were considered (total of 10 tissues).	Cylindrical 25 cm^2 . Homogeneous conductivity: 0.3 S/m .	Anode over C3 and cathode over Fp2.	Type (1) and (3). Studies E-field distribution in 24 head models. Reports significant differences in magnitude and E-field distribution across subjects. States that CSF and brain geometry are factors that explain these differences and that age is the only external factor that had a significant effect on results.
42. Salvador et al. (2015)	Same as (25). GM-WM anisotropy was included.	Rectangular: $5 \times 7 \text{ cm}^2$. Cylindrical $\pi \text{ cm}^2$. Homogeneous conductivity: 2 S/m .	Anode (rectangular or cylindrical) over C3 and rectangular cathode over right SO. The rectangular anode was oriented as in (25).	Type (1) and (3). Compares the E-field distribution of tDCS and TMS of the motor cortex. Reports significant E-field differences in direction, magnitude and location of maxima.
43. Schmidt et al. (2015)	Does a sensitivity analysis varying the conductivities of 4 of the 5 represented tissues: $\sigma_{Scalp} = 0.280 - 0.575 \text{ S/m}$ $\sigma_{Skull} = 0.0016 - 0.0173 \text{ S/m}$ $\sigma_{CSF} = 1.79 \text{ S/m}$ $\sigma_{GM} = 0.220 - 0.445 \text{ S/m}$ $\sigma_{WM} = 0.090 - 0.190 \text{ S/m}$ Isotropic.	No details provided.	74 possible electrode positions (extended 10/10 system). An optimization scheme was used for auditory cortex stimulation.	Type (1), (3) and (6). Optimization scheme to induce a field radial to the cortical target in the auditory cortex. The influence of tissue conductivity in this optimization scheme was studied.
44. Galletta et al. (2015)	Same as (12) (without “synthetic” neck-shoulder region). Includes stroke lesions modelled as CSF.	Rectangular: $5 \times 7 \text{ cm}^2$. Modelled as in (7).	Anode over CP5/F5 and cathode over RSO. Anode over CP6/F6 and cathode over LSO. Anode over F5 and cathode over F6.	Type (3) and (4). Study of tDCS montages used to promote recovery of post-stroke aphasia.

(continued)

Table 9.1 (continued)

Reference	Tissues represented	Electrodes	Montages	Study description / Additional comments
45. Parazzini et al. (2016)	$\sigma_{Scalp} = 0.43 S/m$ $\sigma_{Skull} = 0.015 S/m$ $\sigma_{CSF} = 1.79 S/m$ $\sigma_{GM} = 0.32 S/m$ $\sigma_{WM} = 0.15 S/m$ Isotropic.	17.5 cm long electrode (area of 35 cm ²) that follows approximately the trajectory of the central sulcus. 17.5 cm long electrode (area of 35 cm ²) rounded crown. Rectangular 10x7 cm ² pad. Modelled as in (34).	The long 17.5 cm electrodes were positioned either over M1 or S1. The rectangular electrode was placed over Oz.	Type (1), (2) and (3). Investigates the use of a personalized electrode to modulate the entire extension of the motor / somato-sensitive area.
46. Bortoletto et al. (2016)	Same as (25).	Rectangular: 5 × 7 cm ² . Ring with inner/outer radius of 3.5 cm/4.0 cm. Homogeneous conductivity: 2 S/m.	Same as (25). Central cylindrical anode placed over the FDI region in the LM1. Ring cathode was surrounding it.	Type (2), (3) and (5). Reports higher focality of the radial component of the E-field with the concentric ring configuration.

A priority was given to papers published in international peer reviewed journals, so conference proceedings were ignored unless the work they reported was not found published elsewhere. For notes regarding the classification of the study and the positions of the electrodes, please refer to the bottom of the table

Legend: R/LM1 Right/Left motor cortex, RSO/LSO Right/Left supra-orbital area, L/RDLPFC Left/Right dorsolateral prefrontal cortex, LIFG Left inferior frontal gyrus, STG Superior temporal gyrus, FDI First dorsal interosseous, TPJ Temporoparietal junction, C1, C3/4, Cz, Fp2, FC1, FC3, O1, Oz, T5, T7/8, TP7/8, F3/4, F8, CP1, CP3, CP5/6, P7/8 Positions of the 10–10 international system

Classification:

Type (1): Basic principles of E-field distribution in tDCS: influence of tissue dielectric properties (including anisotropy), electrode modelling, tissue thickness, tissue heating...

Type (2): Study of electrode design: study of a particular electrode design for improving focality of field for a specific application

Type (3): Study of E-field distribution in well-known montages for specific applications

Type (4): Study of tDCS in possible susceptible populations: stroke, obese, children, subjects with skull openings, ...

Type (5): Modelling study integrated in study involving trials with subjects

Type (6): Electrode montage optimization

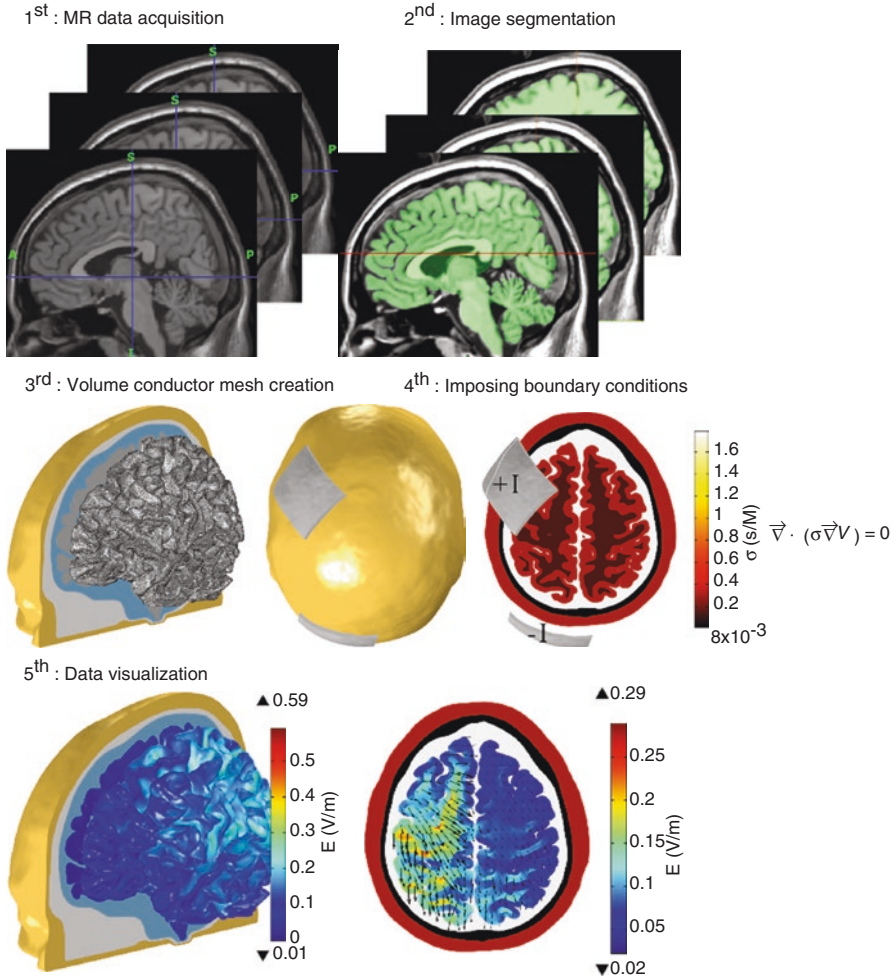


Fig. 9.1 Modeling steps involved in the creation of a computational high-resolution model of the E-field induced in tDCS

properties of the E-field induced in susceptible populations (more on this in section “Use of Computational Models in Clinical Practice”).

The majority of studies shown in Table 9.1 employ a numerical technique known as the finite element method (FEM) to solve the governing physical equations that determine the E-field induced in tDCS (i.e., Laplace’s equation) (Johnson 1997). The FEM yields an approximate numerical solution to a specific equation (or set of equations) that specifies a physical problem in a geometry. In the FEM, the geometry is subdivided into a number of finite elements of a specific shape that are connected by nodes. The latter comprise the finite element’s mesh. Within each element of the mesh, the solution to the equation can be written in terms of an interpolation function

whose parameters depend on the values of the dependent variable in the nodes of each element. In the case of tDCS, the dependent variable is V , the electrostatic potential, and its gradient yields the electric field vector, E . By approximating the solution to the equation with an interpolation function in every element of the mesh, the original equation can be rewritten as a linear equation of the form $\mathbf{AV} = \mathbf{b}$, where \mathbf{A} is a matrix (whose values depend on the geometry of the mesh and the type of elements used), \mathbf{V} is the column vector with the values of the dependent variable (electrostatic potential) in each node of the mesh and \mathbf{b} is another column vector whose values depend on the boundary conditions of the problem (for instance the current injected at each electrode). In order to obtain the column vector \mathbf{V} , it is necessary to invert matrix \mathbf{A} , which can be performed using a number of numerical algorithms.

The first step for creating computational tDCS models is the specification of the geometry of the volume conductor, i.e., the head and electrodes. In most recent studies this is achieved by segmentation of structural magnetic resonance (MR) images, thus obtaining masks, i.e., the set of voxels labeled as belonging to a specific tissue. The choice of MR over other image modalities, such as computed tomography (CT), is mainly related to the fact that it does not involve ionizing radiation. It also offers a higher contrast between soft tissues, such as grey matter (GM) and white matter (WM) and the possibility for molecular phenomena to be observed (e.g. diffusion weighted imaging) (Bashir et al. 2015). MR also has some limitations, however, like the fact that the skull emits a very weak MR signal, therefore making its reconstruction difficult (Windhoff et al. 2013). Most studies use T1-weighted MR images with an isotropic resolution of 1 mm (lower resolutions are sometimes used), although other studies have employed T2 and even PD-weighted images to allow for a better segmentation of the CSF and skull (Miranda et al. 2013; Windhoff et al. 2013). A variety of algorithms and software are described in the literature in order to perform the automatic segmentation of the images. However, manual inspection of the resulting masks and manual segmentation of some structures is often reported as well. The majority of studies produce segmentation masks for the skin, skull, CSF compartments, GM and WM, but others include many more tissues such as muscle, subdermal fat, and eye sclera (Shahid et al. 2013). A number of studies segment the skull into compact and spongy bone (Laakso et al. 2015; Opitz et al. 2015; Rampersad et al. 2012; Saturnino et al. 2015; Wagner et al. 2014a, b). MR images do not usually allow for these two tissues to be segmented, so manual methods (Opitz et al. 2015) or custom MR sequences (Rampersad et al. 2014) are employed.

Generation of the finite element mesh from the segmentation masks is performed using several possible software and algorithms. Three aspects related to the mesh are noteworthy. The first one is its resolution, i.e. the mean distance between the nodes in the mesh. The mesh must have sufficient resolution to accurately predict the spatial distribution of the E-field. The second aspect is the type of element, i.e. the geometry of the finite element. Tetrahedra are often used because they allow for easier compliance to complex curved geometries. However, meshes with hexaedra are described in some studies (Laakso et al. 2015; Sadleir et al. 2010). Tetrahedral meshes are more time consuming to produce, since they require that smooth triangulated surfaces be built for each mask. These surfaces are then used to generate the

volume meshes. Hexahedral meshes can be built directly from the masks, but they do not allow for smooth tissue boundaries to be represented. The only study that was found that compares these two types of meshes (Indahlastari and Sadleir 2015), focused on differences between mean values of the current density in predefined volumes. The differences on the direction of the E-field, however, remain unclear. The third aspect is the quality of the elements in the mesh, which is related to the shape of the elements. Elements with low quality, i.e. elongated elements with very small or very large angles (Windhoff et al. 2013), may lead to numerical instabilities in the FEM. The impact of mesh size and quality is of paramount importance to the obtained E-field results, but remains largely unaddressed in studies published up until now. This is in part due to the complexity of the head geometry, which makes a systematic study of the impact of the mesh challenging.

The stimulating electrodes are accommodated in the model by modifying the scalp's volume mesh. The latter can have different geometries and can be modeled with different degrees of complexity (see Table 9.1). Most models represent the electrodes as homogeneous patches with uniform conductivities (Miranda et al. 2013; Sadleir et al. 2010; Wagner et al. 2007) or as two layers of materials with different conductivities (metal on top of conductive gel) (Datta et al. 2009a). However, recent studies have shown the importance of accurately modeling the geometry of the electrodes, including the presence of a rubber pad inside the saline soaked sponge (sock-electrodes) and accounting for the position of the metal connector in the electrode (Saturnino et al. 2015).

Once the finite element mesh is obtained, the electric conductivity of each tissue and the boundary conditions must be set. The skin and CSF compartments are usually modeled as homogeneous and isotropic. In most models, the GM, WM and cerebellum are also modeled as such, but several studies use diffusion weighted (DW) MR to estimate the diffusion tensor and assign a conductivity tensor for these tissues (Metwally et al. 2015; Oostendorp et al. 2008; Opitz et al. 2015; Rampersad et al. 2014; Sadleir et al. 2010; Salvador et al. 2015; Schmidt et al. 2015; Shahid et al. 2013, 2014; Suh et al. 2012; Wagner et al. 2014a, b), thus allowing for the anisotropy to be taken into account. The skull can either be modeled as isotropic (single layer or three layers, when spongy bone and compact bone are segmented) or as anisotropic (with a single layer) (Rampersad et al. 2012). Conductivity values for DC or low frequencies can be found in a number of recent studies in the literature (Gabriel et al. 1996; Wagner et al. 2014a, b). However, the results are sometimes in disagreement with older data (more on this in the next section). The conductivity of the electrodes/conductive gel/conductive rubber in the electrode models is also often unknown. For homogeneous electrodes this seems to have a limited effect on the results (Opitz et al. 2015), but for more complex electrode models, this can significantly affect the E-field distribution (Saturnino et al. 2015). Other important boundary conditions specify the currents injected by each electrode. This is performed by adjusting the difference between the electric potential of the electrodes (upper boundary of the electrodes in simple electrode models or the metal connector in more realistic models), until the desired current is obtained.

The next step in these models involves inverting the matrix \mathbf{A} , therefore obtaining the values of the potential at each node of the mesh. Since these models can have more than ten million degrees of freedom (nodes), iterative procedures are usually employed (Barrett et al. 1993). These have been shown to provide solutions that have a small error with respect to analytical solutions (Faria et al. 2011). This form of validation, i.e. comparing the results of models with the numerical solution of the E-field, can only be performed in simpler geometrical models, when analytical solutions can be obtained (Ferdjallah et al. 1996; Rush and Driscoll 1968). It also does not allow for a validation of the model *per se*, since many simplifications are introduced related to the geometry of the volume conductor (head) and the electric properties of the tissues. The latter likely affect the predictions of these models much more than numerical inaccuracies.

The final step of the pipeline illustrated in Fig. 9.1 involves the visualization of the E-field distribution and its analysis. This is a crucial step as it will directly influence any clinical decision made about dose. These types of models allow for volume or surface data to be analyzed. Volume data can be processed to yield mean/maximum E-field magnitude values in regions of interest (ROI). Mean E-field values are preferred because they are less sensitive to variations in element size or low-quality elements in the mesh. Surface data can be used to extract information regarding the orientation of the field, particularly in directions perpendicular to the surface (normal component) and tangential to it (tangential component). Analysis of surface data must be performed with care, as the normal component of the E-field is discontinuous across interfaces between tissues (Miranda et al. 2013). In order to further aid the visualization of the results, methods of cortical surface inflation have also been proposed (Laakso et al. 2015; Opitz et al. 2015), since they allow for an easier identification of the E-field maxima at the bottoms of sulci (Miranda et al. 2013). Another challenge lies in the comparison of E-field distributions across subjects, as inter-individual anatomical variability render direct comparisons non-trivial. One interesting solution that has been proposed is to register the individual models to a common atlas (Laakso et al. 2015).

Limitations of State-of-the-Art Computational Models

Computational models based on segmented structural MR images remain the only viable alternative to predict the E-field as a function of the dose parameters. However, they present limitations that can significantly affect the accuracy of their predictions. The first limitation is related to the inherent difficulties associated with segmentation of certain tissues in MR images. As mentioned previously, the skull and the CSF are particularly difficult to segment from T1/T2 images, and thus require manual corrections, or the use of specific image acquisition parameters that are not commonly used in a clinical setting. However, correctly modeling these tissues is critical to achieving accurate predictions, particularly because the largest change in electrical conductivity occurs precisely at the skull-CSF border. Many studies have shown the impact of the

skull modeling (Opitz et al. 2015; Rampersad et al. 2012) and of the thickness of the CSF layer on the electric field in the brain (i.e., cortical regions where the CSF is thin have a significantly higher E-field magnitude, (Opitz et al. 2015)).

The geometry of the head models is usually obtained from MR images of a single individual. This can significantly bias the obtained E-field distribution, since great anatomical variations can exist between individuals (Huang et al. 2016). The effects of these differences have been addressed in a number of studies (Datta et al. 2012; Laakso et al. 2015). One alternative is to create individualized models for each participant in a given study, but this is difficult due to the high computational resources and specific know-how required to build such models. One other option is to use a volume conductor geometry that is obtained from averaged MR images of a number of individuals (Huang et al. 2016). This makes the particular features of the geometry of the volume conductor less susceptible to individual features of a single head but might be less representative for a specific individual (i.e., patients or research subjects).

One large difference between studies lies in the way the electrical conductivity of tissues is modeled, and which values are assigned to it. This can be clearly seen by the sometimes great disparity between the conductivity values assigned to the different tissues (see the second column of Table 9.1). Since this greatly affects the predictions of computational models, some studies have conducted sensitivity analyses on the values of the isotropic conductivities or the effects of the presence of skull and/or WM anisotropy (Laakso et al. 2015; Metwally et al. 2015; Schmidt et al. 2015; Shahid et al. 2013, 2014; Suh et al. 2012; Wagner et al. 2014a, b). No “gold standard” exists nowadays for a way to model the electrical properties of tissues in the DC range of frequencies, so care must be taken when comparing predictions between studies that employ different settings.

Another important limitation of computational models is that the information they provide is hampered by the lack of knowledge about the precise mechanisms of interaction of the E-field with the neurons. In other words, much is still unclear about how the information obtained from these computational models about the magnitude and direction of the E-field translates into modulation of the electrical activity of neurons. At first this may sound paradoxical, since the fundamentals of the E-field interaction with single neurons have been known for a long time (see Chap. 2 and (Roth 1994) for a review). In summary, polarization will occur in regions of maximum value of the activation function (gradient along the neuron of the E-field parallel to the neuron’s trajectory) (Rattay 1986). At the scale of cortical neurons, the gradient of the E-field along the neuron is small, but strong polarizations can occur in regions where the axon or dendritic tree processes bend or terminate (Amassian et al. 1992; Nagarajan et al. 1993) as well as on the soma (Rahman et al. 2013).

The existence of several potential interaction mechanisms, together with the fact that the actual geometry of the neurons is rather complex, makes predictions about sites of activation and the components of the E-field more likely to influence them hard to make. One generally adopted approximation that has been proposed to solve this is to assume that the polarization of the neurons will be proportional to the

E-field's magnitude. This is termed the “quasi-uniform” assumption (Bikson et al. 2013) and similar approximations have been proposed before in other forms of stimulation, such as TMS (Ruohonen 1998). The E-field's component in a direction either perpendicular (radial) or tangential to the cortical sheet may also be explicitly computed (Faria et al. 2011) and might be the relevant factor in determining the field's interaction with neurons. The radial component of the E-field optimally polarize pyramidal cells in the cortex with dendrites that extend normal to the surface (Bikson et al. 2004; Datta et al. 2008). It also easily explains the polarity dependent nature of the neuro-modulatory effects elicited by tDCS that is observed up to a certain value of current intensity (Merlet et al. 2013; Nitsche and Paulus 2000). Tangential E-fields would optimally polarize axon afferents projecting along the surface (Rahman et al. 2013). The quasi-uniform assumption does not model neuron specific effects (Radman et al. 2009) or consider the role of changes in electric fields, as notably occurs across the grey-white matter interface (Miranda et al. 2003, 2007; Salvador et al. 2011).

Use of Computational Models in Clinical Practice

Optimizing Efficacy

Since the early days of tDCS, many options regarding dose parameters have been chosen on a trial-and-error basis. As an example, consider the original study by Nitsche and Paulus (Nitsche and Paulus 2000), which demonstrated that tDCS could elicit long lasting excitability changes in the motor cortex, by placing one electrode over the primary motor cortex and the other over the contralateral supraorbital area (M1-SO montage). In that study, the authors reported several other bipolar electrode configurations that were tested and that failed to elicit the same results. While in some follow-up studies these canonical results were interpreted as suggesting that current flow in the M1-SO montage affected mostly the motor region- and by extension that tDCS could be focalized to any region by placing a large pad electrode over it – it is important to recognize that such an interpretation was not implied by the authors of the original study.

The recent computational studies that have emerged provide useful insights into the E-field distribution in the brain that can aid in optimizing the efficacy in clinical applications of tDCS. Many of the initial computational studies aimed at clarifying the E-field distribution in realistic representations of electrode montages used in clinical practice in a series of applications (Datta et al. 2009a; Miranda et al. 2013; Sadleir et al. 2010). In contrast to earlier models based on concentric spheres (Miranda et al. 2006; Rush and Driscoll 1968) or abstracted geometry (CAD, (Wagner et al. 2007)), a critical feature of models applied since ~2009 is the incorporation of “gyri-precise” resolution based on precise anatomical MRI scans, and attention to continuity of CSF involving smoothing beyond scan resolution. This level of detail resulted in several key predictions that challenged prevailing views on dose design: (1) significant current flow occurs between (rather than simply under) electrodes; (2) current is clustered in hot-spots whose locations depend on idiosyn-

cratic anatomy; (3) both electrodes are functional regardless of position (including extracephalic or “supra-orbital) and current under each electrode is influenced by the position of the others (Bikson et al. 2010). It should be noted that even as modeling technology has continued to evolve (e.g. addition of anisotropy; (Oostendorp et al. 2008; Suh et al. 2009)), and despite variation in methods (e.g. conductivity, (Opitz et al. 2015)), these basic predictions remain largely intact over the last 7 years of intensive modeling studies. In fact, it is precisely because current flow is not intuitive that models are important tools in the interpretation and design of tDCS studies.

These high-resolution studies proved useful in determining which regions were targeted by these configurations and what was the direction of the induced E-field in different regions. Based on the latter, a newer batch of studies has appeared geared towards optimizing multi-electrode montages to achieve a target E-field distribution and orientation in pre-defined cortical regions of interest (Dmochowski et al. 2011; Ruffini et al. 2014; Sadleir et al. 2012). They use the superposition principle, i.e., the principle that the E-field distribution in the head induced by a given set of electrodes can be obtained by the weighted sum of the E-fields induced by bipolar electrode configurations with a common return electrode. The weights used to sum the bipolar induced E-field configurations are the currents set in each electrode of the multi-electrode configuration. These types of models then determine the current intensity applied at each electrode (placed in a predefined array of positions) such that the induced E-field best approximates a pre-defined target E-field distribution in the brain. This optimization procedure can be further constrained by imposing maximum values for the current on each electrode and the total injected current.

The main difference between the implementations in each study is related to the components of the E-field which were optimized (pre-determined E-field with any desired direction, as specified by the user (Dmochowski et al. 2011), E-field component radial to the cortical sheet in (Ruffini et al. 2014) or magnitude of the E-field (Sadleir et al. 2012)). Other differences are the algorithms used to minimize the difference between the induced E-field and the target field, and the type of electrodes and pre-defined electrode positions. These studies have shown that it is possible to induce E-fields in target regions with higher focality and/or magnitude than those using conventional approaches (i.e. bipolar “pad-like” electrodes) (Dmochowski et al. 2011). Moreover, they suggest the possibility of using data from functional imaging techniques (electroencephalography, positron emission tomography and functional magnetic resonance imaging) to derive cortical activation maps that may serve as the target E-field distribution that served as input to these studies (Ruffini et al. 2014). Finally, they offer the possibility of avoiding unwanted stimulation of certain regions by minimizing the E-field induced in the latter (Sadleir et al. 2012).

In spite of the usefulness of computational models, their implementation can be a complex task for research groups, particularly those with clinical applications. Working in close collaboration with a computational modeling group might be an alternative, and indeed, many studies nowadays seek to incorporate the information from these models as a rationale to dose parameter decisions and/or as support for

some of the conclusions of the study (see references marked as type (5) in Table 9.1). The creation of tools to allow for easier implementation of these models (Jung et al. 2013; Windhoff et al. 2013) and of databases of models (Truong et al. 2014) can also allow for a wider implementation of computational models as part of the pipeline for experiment design.

Safety and Tolerability Considerations

It is not trivial to translate the predictions of computational E-field calculations to statements about safety or tolerability of a specific dose selection in tDCS. This occurs because, while the E-field distribution in tDCS can be predicted from these models in different tissues, the relation between the field and potential unwanted side-effects are not well known. None-the-less, under the assumption that increasing the E-field in a given target increases the theoretical risk of injury, even by providing comparative electric field across montages and subject populations (e.g. pediatric, stroke, injury), models are a valuable tool to assess risk.

One aspect related to tolerability, for instance, are the reported tingling and itching sensations under the electrodes and the acute erythema that has been associated with vasodilation (Woods et al. 2016). Computational models allow for the E-field in the skin-electrode interface to be calculated, and complex electrode models incorporating the gel and conductive rubber pads within saline soaked electrodes have been produced (Saturnino et al. 2015). These calculations, however, are of limited application since no model exists at the moment to relate the E-field to the reported undesired effects.

Regarding safety issues, attention has focused on predicting the electric field (current density) threshold at which injury may occur in the brain, skin or other structures. This work has, in turn, relied on injury thresholds proposed by animal models – which generally suggest thresholds more than one order of magnitude above clinical tDCS intensities. Computational models are essential to make scaling of intensities between animal models and humans more precise for this purpose, because for the same applied current or current density at electrodes, the resulting electric fields in rodent are much higher than those in human. For instance, injuries linked to possible tissue damage caused by heating (joule heating) may be relevant to tDCS. This has been addressed in a study (Datta et al. 2009b) which has shown that application of tDCS with a current to electrode area ratio of 142.9 A/m², a value that has been shown to lead to lesions in *in vivo* rat models (Liebetanz et al. 2009), caused a small maximum temperature increase in the brain (0.55 °C) but a significant scalp temperature increase (14.68 °C). However, these models require validation and many important factors, like sweat gland response in the scalp, were not modeled.

Another important safety issue is related to the usage of extracephalic return electrodes, which have been proposed to avert unwanted effects of tDCS in cortical areas away from the target region (Moliadze et al. 2010). However, modeling studies

showed that use of extracephalic electrodes does not “cancel” the role of the return electrode, but rather creates extensive current flow through the foramen magnum, thereby affecting deep and mid-brain structures (Datta et al. 2011). It was speculated that current flow produced by extracephalic electrodes might interfere with other excitable tissues in the brainstem or the heart, which can lead to severe complications. Studies addressing this (Parazzini et al. 2013a, b) calculated current density magnitudes in these tissues and compared them to reported threshold values for cardiac fibrillation or with values induced in the brainstem during conventional bipolar montages, as these do not show unwanted brainstem neuromodulatory effects. These approaches to assess the lack of unwanted effects of the induced E-field still have some potential shortcomings, however, since the direction of the E-field is also a factor influencing neuronal stimulation and this aspect is not taken into account when analyzing only the magnitude of the field. One alternative to the use of extracephalic electrodes is the use of the multi-electrode optimization approaches that were mentioned in the last section, which may allow for a reduction of the unwanted secondary activations in unwanted brain areas. The latter also allows for the current in each electrode and the total overall current to be limited to specified maximum values.

The use of tDCS in subjects with skull defects (Datta et al. 2010) or in children (Gillick et al. 2014; Kessler et al. 2013; Minhas et al. 2012; Parazzini et al. 2014a) is also a matter that warrants caution, since the E-field distribution in these populations may be significantly different from that in healthy adult subjects. The presence of skull holes, for instance, was found to significantly increase the E-field if the electrode is placed directly on top of it. Regarding pediatric tDCS applications, the E-field induced in the child brain was found to be on average higher than that induced in adult brain using the same dose parameters. These results support the importance of carefully studying the E-field distribution in these models and leveraging them as a means to adjust dose parameters.

Dose Selection on an Individual Basis

Currently, the technical sophistication required to generate high-resolution computational models make implementation on a subject specific basis a very time-consuming process. Recent efforts have aimed to automate the individual segmentation process in a manner that does not compromise model precision (Huang and Parra 2015). Typically, however, computational studies involve the creation of one head model and the generalization of the results to other head geometries. This approach works well when the study’s goal is to determine basic principles of the spatial distribution of the E-field in tDCS. A few modeling studies have studied the impact of intersubject variability in the E-field distribution in tDCS (Datta et al. 2012; Laakso et al. 2015). These studies report significant differences arising from details in the geometry of the cortical sheet. One of these studies reports that the E-field in the hand motor area across 24 individual subjects followed a normal distribution with a standard deviation of about 20% of the mean (Laakso et al. 2015). Recently, a

standardized head based on the MNI has been developed specifically for tDCS modeling, and has been shown to provide reasonable predictions of individualized subject response (Huang et al. 2016).

Other examples of cases warranting individualized head models are studies involving stroke patients, for which the size of the lesion and its location and shape can significantly affect the distribution of the induced E-field (Datta et al. 2011). Other examples are the already mentioned studies involving children (Minhas et al. 2012) or studies involving obese subjects (Truong et al. 2013). In those cases, individualized models remain the only viable way to provide a realistic E-field distribution and thus optimize dose parameters (Dmochowski et al. 2013).

Examples of Application of Computational Modeling in Case Studies

Computational models of tDCS can be performed proactively or retroactively. Proactive modeling can influence montage selection by informing researchers of stimulation focality and intensity for a region of interest. In atypical case studies, safety concerns can be assessed and mitigated by proactively modeling the stimulation protocol and comparing to a typical subject. Examples of this strategy include pediatrics, stroke, and subjects with cranial defects (Bikson et al. 2016; Minhas et al. 2012). In Fig. 9.2, tDCS is simulated in a subject with and without idealized Deep Brain Stimulation (DBS) leads. As an extreme case, the burrhole defect typical in subthalamic nucleus DBS is allowed to be fluid filled and relatively conductive. Common sponge (conventional) and HD-tDCS montages for motor and cerebellar stimulation are compared. Fluid filled burrholes draw a greater amount of current density than what would normally exist with healthy tissue (dashed images). However, peak current density and electric field are minimally affected (less than twofold). In general, HD configurations exhibit lower electric field intensities in deep brain structures while exhibiting more focal field patterns.

While tDCS modeling tools are becoming more accessible (COMETS, Bonsai, SimNIBS) (Jung et al. 2013; Thielscher et al. 2015; Truong et al. 2014) many transcranial stimulation studies have been and are performed without the guidance of modeling. Retroactive modeling of a specific study's stimulation parameters can help to resolve mechanisms of action or explain variance within or between studies. Fig. 9.3 represents a post-hoc analysis of common tDCS montages used in schizophrenia (Brunelin et al. 2012; Shiozawa et al. 2013). The electric field magnitude on the cortical surface depicts regions of maximum stimulation regardless of field orientation (A). The radial component of the electric field predicts the effects of stimulation on layer V pyramidal neurons aligned perpendicular to the cortical surface (B). Field orientation, anodal (red) or cathodal (blue), is commonly postulated to have excitatory or inhibitory effects on local regions (B). Meanwhile, tangential electric field magnitude is predicted to affect local connections oriented along the cortical surface (C).

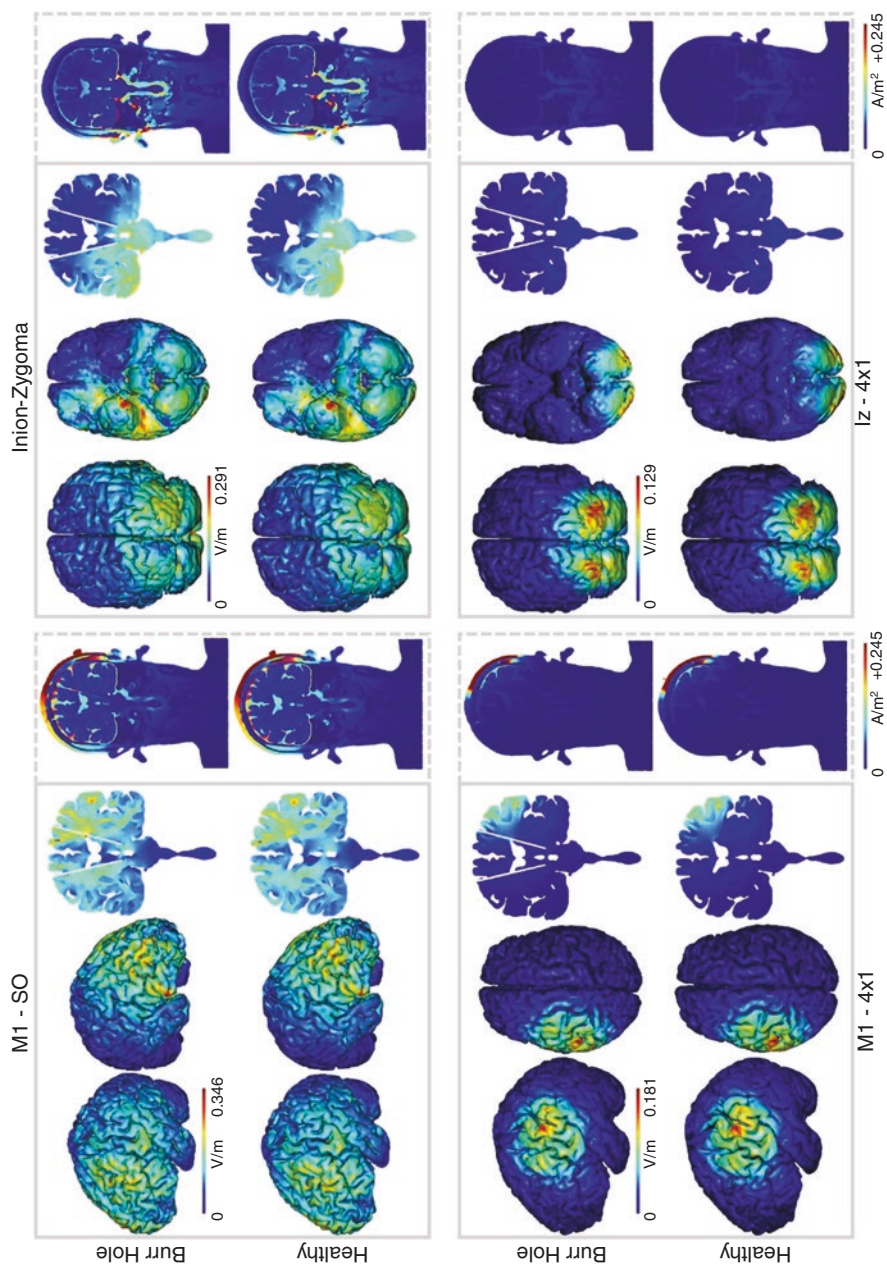


Fig. 9.2 Simulation of tDCS in subjects with idealized Deep Brain Stimulation (DBS) leads using conventional 5 x 7 cm sponge and HD (4 x 1) montages

References

- Amassian, V. E., Eberle, L., Maccabee, P. J., & Cracco, R. Q. (1992). Modelling magnetic coil excitation of human cerebral cortex with a peripheral nerve immersed in a brain-shaped volume conductor: The significance of fiber bending in excitation. *Electroencephalography and Clinical Neurophysiology*, *85*(5), 291–301.
- Barrett, R., Berry, M., Chan, T. F., Demmel, J., Donato, J. M., Dongarra, J., ... Van der Vorst, H. (1993). *Templates for the solution of linear systems: Building blocks for iterative methods* (2nd ed.). Philadelphia, PA: Society for Industrial and Applied Mathematics.
- Bashir, U., Mallia, A., Stirling, J., Joemon, J., MacKewn, J., Charles-Edwards, G., ... Cook, G. J. (2015). PET/MRI in oncological imaging: State of the art. *Diagnostica*, *5*(3), 333–357.
- Bikson, M., Datta, A., Rahman, A., & Scaturro, J. (2010). Electrode montages for tDCS and weak transcranial electrical stimulation: Role of “return” electrode’s position and size. *Clinical Neurophysiology*, *121*(12), 1976–1978.
- Bikson, M., Dmochowski, J., & Rahman, A. (2013). The “quasi-uniform” assumption in animal and computational models of non-invasive electrical stimulation. *Brain Stimulation*, *6*(4), 704–705.
- Bikson, M., Grossman, P., Thomas, C., Zannou, A. L., Jiang, J., Adnan, T., ... Woods, A. J. (2016). Safety of transcranial direct current stimulation: Evidence based update 2016. *Brain Stimulation*, *9*(5), 641–661.
- Bikson, M., Inoue, M., Akiyama, H., Deans, J. K., Fox, J. E., Miyakawa, H., & Jefferys, J. G. (2004). Effects of uniform extracellular DC electric fields on excitability in rat hippocampal slices in vitro. *The Journal of Physiology*, *557*(Pt 1), 175–190.
- Bortoletto, M., Rodella, C., Salvador, R., Miranda, P. C., & Miniussi, C. (2016). Reduced current spread by concentric electrodes in transcranial electrical stimulation (tES). *Brain Stimulation*, *9*(4), 525–528.
- Brunelin, J., Mondino, M., Gassab, L., Haesebaert, F., Gaha, L., Suaud-Chagny, M. F., ... Poulet, E. (2012). Examining transcranial direct-current stimulation (tDCS) as a treatment for hallucinations in schizophrenia. *The American Journal of Psychiatry*, *169*(7), 719–724.
- Brunoni, A. R., Shiozawa, P., Truong, D., Javitt, D. C., Elkis, H., Fregni, F., ... Bikson, M. (2014). Understanding tDCS effects in schizophrenia: A systematic review of clinical data and an integrated computation modeling analysis. *Expert Review of Medical Devices*, *11*(4), 383–394.
- Dasilva, A. F., Mendonca, M. E., Zaghi, S., Lopes, M., Dossantos, M. F., Spierings, E. L., ... Fregni, F. (2012). tDCS-induced analgesia and electrical fields in pain-related neural networks in chronic migraine. *Headache*, *52*(8), 1283–1295.
- Datta, A., Baker, J. M., Bikson, M., & Fridriksson, J. (2011). Individualized model predicts brain current flow during transcranial direct-current stimulation treatment in responsive stroke patient. *Brain Stimulation*, *4*(3), 6.
- Datta, A., Bansal, V., Diaz, J., Patel, J., Reato, D., & Bikson, M. (2009a). Gyri-precise head model of transcranial direct current stimulation: Improved spatial focality using a ring electrode versus conventional rectangular pad. *Brain Stimulation*, *2*(4), 201–207.
- Datta, A., Bikson, M., & Fregni, F. (2010). Transcranial direct current stimulation in patients with skull defects and skull plates: High-resolution computational FEM study of factors altering cortical current flow. *NeuroImage*, *52*(4), 1268–1278.
- Datta, A., Elwassif, M., Battaglia, F., & Bikson, M. (2008). Transcranial current stimulation focality using disc and ring electrode configurations: FEM analysis. *Journal of Neural Engineering*, *5*(2), 163–174.
- Datta, A., Elwassif, M., & Bikson, M. (2009b). *Bio-heat transfer model of transcranial DC stimulation: Comparison of conventional pad versus ring electrode*. Paper presented at the 31st annual international conference of the IEEE engineering in medicine and biology society (EMBC), Minneapolis.

- Datta, A., Krause, M. R., Pilly, P. K., Choe, J., Zanos, T. P., Thomas, C., & Pack, C. C. (2016). *On comparing in vivo intracranial recordings in non-human primates to predictions of optimized transcranial electrical stimulation*. Paper presented at the 36th Annual International Conference of the IEEE Engineering in Medicine and Biology Society (EMBC), Orlando.
- Datta, A., Truong, D., Minhas, P., Parra, L. C., & Bikson, M. (2012). Inter-individual variation during transcranial direct current stimulation and normalization of dose using MRI-derived computational models. *Frontiers in Psychiatry*, 3, 91.
- Dmochowski, J. P., Datta, A., Bikson, M., Su, Y. Z., & Parra, L. C. (2011). Optimized multi-electrode stimulation increases focality and intensity at target. *Journal of Neural Engineering*, 8(4), 046011.
- Dmochowski, J. P., Datta, A., Huang, Y., Richardson, J. D., Bikson, M., Fridriksson, J., & Parra, L. C. (2013). Targeted transcranial direct current stimulation for rehabilitation after stroke. *NeuroImage*, 75, 12–19.
- Dymond, A. M., Coger, R. W., & Serafetinides, E. A. (1975). Intracerebral current levels in man during electrosleep therapy. *Biological Psychiatry*, 10(1), 101–104.
- Eaton, H. (1992). Electric field induced in a spherical volume conductor from arbitrary coils: Application to magnetic stimulation and MEG. *Medical & Biological Engineering & Computing*, 30(4), 433–440.
- Faria, P., Hallett, M., & Miranda, P. C. (2011). A finite element analysis of the effect of electrode area and inter-electrode distance on the spatial distribution of the current density in tDCS. *Journal of Neural Engineering*, 8(6), 066017.
- Ferdjallah, M., Bostick, F. X., Jr., & Barr, R. E. (1996). Potential and current density distributions of cranial electrotherapy stimulation (CES) in a four-concentric-spheres model. *IEEE Transactions on Biomedical Engineering*, 43(9), 939–943.
- Gabriel, C., Gabriel, S., & Corthout, E. (1996). The dielectric properties of biological tissues: I. Literature survey. *Physics in Medicine and Biology*, 41(11), 2231–2249.
- Galletta, E. E., Cancelli, A., Cottone, C., Simonelli, I., Tecchio, F., Bikson, M., & Marangolo, P. (2015). Use of computational modeling to inform tDCS electrode montages for the promotion of language recovery in post-stroke aphasia. *Brain Stimulation*, 8(6), 1108–1115.
- Gillick, B. T., Kirton, A., Carmel, J. B., Minhas, P., & Bikson, M. (2014). Pediatric stroke and transcranial direct current stimulation: Methods for rational individualized dose optimization. *Frontiers in Human Neuroscience*, 8, 739.
- Halko, M. A., Datta, A., Plow, E. B., Scaturro, J., Bikson, M., & Merabet, L. B. (2011). Neuroplastic changes following rehabilitative training correlate with regional electrical field induced with tDCS. *NeuroImage*, 57(3), 885–891.
- Huang, Y., & Parra, L. C. (2015). Fully automated whole-head segmentation with improved smoothness and continuity, with theory reviewed. *PLoS One*, 10(5), e0125477.
- Huang, Y., Parra, L. C., & Haufe, S. (2016). The New York head-a precise standardized volume conductor model for EEG source localization and tES targeting. *NeuroImage*, 140, 150–162.
- Indahlastari, A., & Sadleir, R. J. (2015). *A comparison between block and smooth modeling in finite element simulations of tDCS*. Paper presented at the 37th annual international conference of the IEEE engineering in medicine and biology society (EMBC), Milan.
- Johnson, C. R. (1997). Computational and numerical methods for bioelectric field problems. *Critical Reviews in Biomedical Engineering*, 25(1), 1–81.
- Jung, Y.-J., Kim, J.-H., & Im, C.-H. (2013). COMETS: A MATLAB toolbox for simulating local electric fields generated by transcranial direct current stimulation (tDCS). [journal article]. *Biomedical Engineering Letters*, 3(1), 39–46.
- Kessler, S. K., Minhas, P., Woods, A. J., Rosen, A., Gorman, C., & Bikson, M. (2013). Dosage considerations for transcranial direct current stimulation in children: A computational modeling study. *PLoS One*, 8(9), e76112.
- Laakso, I., Tanaka, S., Koyama, S., De Santis, V., & Hirata, A. (2015). Inter-subject variability in electric fields of motor cortical tDCS. *Brain Stimulation*, 8(5), 8.

- Liebetanz, D., Koch, R., Mayenfels, S., Konig, F., Paulus, W., & Nitsche, M. A. (2009). Safety limits of cathodal transcranial direct current stimulation in rats. *Clinical Neurophysiology*, *120*(6), 1161–1167.
- Lopez-Alonso, V., Cheeran, B., Rio-Rodriguez, D., & Fernandez-Del-Olmo, M. (2014). Inter-individual variability in response to non-invasive brain stimulation paradigms. *Brain Stimulation*, *7*(3), 372–380.
- Mendonca, M. E., Santana, M. B., Baptista, A. F., Datta, A., Bikson, M., Fregni, F., & Araujo, C. P. (2011). Transcranial DC stimulation in fibromyalgia: Optimized cortical target supported by high-resolution computational models. *The Journal of Pain*, *12*(5), 610–617.
- Merlet, I., Birot, G., Salvador, R., Molaee-Ardekani, B., Mekonnen, A., Soria-Frisch, A., ... Wendling, F. (2013). From oscillatory transcranial current stimulation to scalp EEG changes: A biophysical and physiological modeling study. *PLoS One*, *8*(2), e57330.
- Metwally, M. K., Han, S. M., & Kim, T. S. (2015). The effect of tissue anisotropy on the radial and tangential components of the electric field in transcranial direct current stimulation. *Medical & Biological Engineering & Computing*, *53*(10), 1085–1101.
- Minhas, P., Bikson, M., Woods, A. J., Rosen, A. R., & Kessler, S. K. (2012). *Transcranial direct current stimulation in pediatric brain: A computational modeling study*. Paper presented at the 34th annual international conference of the IEEE engineering in medicine and biology society (EMBC), San Diego.
- Miranda, P. C., Correia, L., Salvador, R., & Basser, P. J. (2007). Tissue heterogeneity as a mechanism for localized neural stimulation by applied electric fields. *Physics in Medicine and Biology*, *52*(18), 5603–5617.
- Miranda, P. C., Hallett, M., & Basser, P. J. (2003). The electric field induced in the brain by magnetic stimulation: A 3-D finite-element analysis of the effect of tissue heterogeneity and anisotropy. *IEEE Transactions on Biomedical Engineering*, *50*(9), 1074–1085.
- Miranda, P. C., Lomarev, M., & Hallett, M. (2006). Modeling the current distribution during transcranial direct current stimulation. *Clinical Neurophysiology*, *117*(7), 1623–1629.
- Miranda, P. C., Mekonnen, A., Salvador, R., & Ruffini, G. (2013). The electric field in the cortex during transcranial current stimulation. *NeuroImage*, *70*, 48–58.
- Moliadze, V., Antal, A., & Paulus, W. (2010). Electrode-distance dependent after-effects of transcranial direct and random noise stimulation with extracephalic reference electrodes. *Clinical Neurophysiology*, *121*(12), 2165–2171.
- Nagarajan, S. S., Durand, D. M., & Warman, E. N. (1993). Effects of induced electric-fields on finite neuronal structures – A simulation study. *IEEE Transactions on Biomedical Engineering*, *40*(11), 1175–1188.
- Nitsche, M. A., & Paulus, W. (2000). Excitability changes induced in the human motor cortex by weak transcranial direct current stimulation. *The Journal of Physiology London*, *527*(3), 633–639.
- Oostendorp, T. F., Hengeveld, Y. A., Wolters, C. H., Stinstra, J., van Elswijk, G., & Stegeman, D. F. (2008). *Modeling transcranial DC stimulation*. Paper presented at the 30th annual international conference of the IEEE engineering in medicine and biology society (EMBC), Vancouver.
- Opitz, A., Falchier, A., Yan, C. G., Yeagle, E. M., Linn, G. S., Megevand, P., ... Schroeder, C. E. (2016). Spatiotemporal structure of intracranial electric fields induced by transcranial electric stimulation in humans and nonhuman primates. *Scientific Reports*, *6*, 31236.
- Opitz, A., Paulus, W., Will, S., Antunes, A., & Thielscher, A. (2015). Determinants of the electric field during transcranial direct current stimulation. *NeuroImage*, *109*, 140–150.
- Parazzini, M., Focchi, S., Cancelli, A., Cottone, C., Liorni, I., Ravazzani, P., & Tecchio, F. (2016). A computational model of the electric field distribution due to regional personalized or non-personalized electrodes to select transcranial electric stimulation target. *IEEE Transactions on Biomedical Engineering*, *64*, 184–195.

- Parazzini, M., Fiocchi, S., Liorni, I., Priori, A., & Ravazzani, P. (2014a). Computational modeling of transcranial direct current stimulation in the child brain: Implications for the treatment of refractory childhood focal epilepsy. *International Journal of Neural Systems*, 24(2), 1430006.
- Parazzini, M., Fiocchi, S., & Ravazzani, P. (2012). Electric field and current density distribution in an anatomical head model during transcranial direct current stimulation for tinnitus treatment. *Bioelectromagnetics*, 33(6), 476–487.
- Parazzini, M., Fiocchi, S., Rossi, E., Paglialonga, A., & Ravazzani, P. (2011). Transcranial direct current stimulation: Estimation of the electric field and of the current density in an anatomical human head model. *IEEE Transactions on Biomedical Engineering*, 58(6), 1773–1780.
- Parazzini, M., Rossi, E., Ferrucci, R., Liorni, I., Priori, A., & Ravazzani, P. (2014b). Modelling the electric field and the current density generated by cerebellar transcranial DC stimulation in humans. *Clinical Neurophysiology*, 125(3), 577–584.
- Parazzini, M., Rossi, E., Rossi, L., Priori, A., & Ravazzani, P. (2013a). Evaluation of the current density in the brainstem during transcranial direct current stimulation with extra-cephalic reference electrode. *Clinical Neurophysiology*, 124(5), 1039–1040.
- Parazzini, M., Rossi, E., Rossi, L., Priori, A., & Ravazzani, P. (2013b). Numerical estimation of the current density in the heart during transcranial direct current stimulation. *Brain Stimulation*, 6(3), 457–459.
- Peterchev, A. V., Wagner, T. A., Miranda, P. C., Nitsche, M. A., Paulus, W., Lisanby, S. H., ... Bikson, M. (2012). Fundamentals of transcranial electric and magnetic stimulation dose: Definition, selection, and reporting practices. *Brain Stimulation*, 5(4), 435–453.
- Radman, T., Ramos, R. L., Brumberg, J. C., & Bikson, M. (2009). Role of cortical cell type and morphology in subthreshold and suprathreshold uniform electric field stimulation in vitro. *Brain Stimulation*, 2(4), 215–228.
- Rahman, A., Reato, D., Arlotti, M., Gasca, F., Datta, A., Parra, L. C., & Bikson, M. (2013). Cellular effects of acute direct current stimulation: Somatic and synaptic terminal effects. *Journal of Physiology London*, 591(10), 2563–2578.
- Rampersad, S., Stegeman, D., & Oostendorp, T. (2012). Single-layer skull approximations perform well in transcranial direct current stimulation modeling. *IEEE Transactions on Neural Systems and Rehabilitation Engineering*, 1(3), 8.
- Rampersad, S. M., Janssen, A. M., Lucka, F., Aydin, U., Lanfer, B., Lew, S., ... Oostendorp, T. F. (2014). Simulating transcranial direct current stimulation with a detailed anisotropic human head model. *IEEE Transactions on Neural Systems and Rehabilitation Engineering*, 22(3), 441–452.
- Rattay, F. (1986). Analysis of models for external stimulation of axons. *IEEE Transactions on Biomedical Engineering*, 33(10), 974–977.
- Roth, B. J. (1994). Mechanisms for electrical-stimulation of excitable tissue. *Critical Reviews in Biomedical Engineering*, 22(3–4), 253–305.
- Roth, B. J., Cohen, L. G., & Hallett, M. (1991). The electric field induced during magnetic stimulation. *Electroencephalography and Clinical Neurophysiology*, 43, 268–278.
- Ruffini, G., Fox, M. D., Ripolles, O., Miranda, P. C., & Pascual-Leone, A. (2014). Optimization of multifocal transcranial current stimulation for weighted cortical pattern targeting from realistic modeling of electric fields. *NeuroImage*, 89, 216–225.
- Ruohonen, J. (1998). *Transcranial magnetic stimulation: Modelling and new techniques*. Unpublished PhD, Helsinki University of Technology, Espoo.
- Rush, S., & Driscoll, D. A. (1968). Current distribution in the brain from surface electrodes. *Anesthesia and Analgesia*, 47(6), 717–723.
- Sadleir, R. J., Vannorsdall, T. D., Schretlen, D. J., & Gordon, B. (2010). Transcranial direct current stimulation (tDCS) in a realistic head model. *NeuroImage*, 51(4), 1310–1318.

- Sadleir, R. J., Vannorsdall, T. D., Schretlen, D. J., & Gordon, B. (2012). Target optimization in transcranial direct current stimulation. *Frontiers in Psychiatry*, 3, 90.
- Salvador, R., Silva, S., Basser, P. J., & Miranda, P. C. (2011). Determining which mechanisms lead to activation in the motor cortex: A modeling study of transcranial magnetic stimulation using realistic stimulus waveforms and sulcal geometry. *Clinical Neurophysiology*, 122(4), 748–758.
- Salvador, R., Wenger, C., & Miranda, P. C. (2015). Investigating the cortical regions involved in MEP modulation in tDCS. [original research]. *Frontiers in Cellular Neuroscience*, 9: 405 (11 pages).
- Saturnino, G. B., Antunes, A., & Thielscher, A. (2015). On the importance of electrode parameters for shaping electric field patterns generated by tDCS. *NeuroImage*, 120, 25–35.
- Schmidt, C., Wagner, S., Burger, M., Rienen, U., & Wolters, C. H. (2015). Impact of uncertain head tissue conductivity in the optimization of transcranial direct current stimulation for an auditory target. *Journal of Neural Engineering*, 12(4), 046028.
- Shahid, S., Wen, P., & Ahfock, T. (2013). Numerical investigation of white matter anisotropic conductivity in defining current distribution under tDCS. *Computer Methods and Programs in Biomedicine*, 109(1), 48–64.
- Shahid, S. S., Bikson, M., Salman, H., Wen, P., & Ahfock, T. (2014). The value and cost of complexity in predictive modelling: Role of tissue anisotropic conductivity and fibre tracts in neuromodulation. *Journal of Neural Engineering*, 11(3), 036002.
- Shiozawa, P., da Silva, M. E., Cordeiro, Q., Fregni, F., & Brunoni, A. R. (2013). Transcranial direct current stimulation (tDCS) for the treatment of persistent visual and auditory hallucinations in schizophrenia: A case study. *Brain Stimulation*, 6(5), 831–833.
- Suh, H. S., Kim, S. H., Lee, W. H., & Kim, T. S. (2009). *Realistic simulation of transcranial direct current stimulation via 3-D high-resolution finite element analysis: Effect of tissue anisotropy*. Paper presented at the 29th annual international conference of the IEEE engineering in medicine and biology society (EMBC), Minneapolis.
- Suh, H. S., Lee, W. H., & Kim, T. S. (2012). Influence of anisotropic conductivity in the skull and white matter on transcranial direct current stimulation via an anatomically realistic finite element head model. *Physics in Medicine and Biology*, 57(21), 6961–6980.
- Thielscher, A., Antunes, A., & Saturnino, G. B. (2015). Field modeling for transcranial magnetic stimulation: A useful tool to understand the physiological effects of TMS? *Conference Proceedings: Annual International Conference of the IEEE Engineering in Medicine and Biology Society*, 2015, 222–225.
- Tofts, P. S. (1990). The distribution of induced currents in magnetic stimulation of the nervous-system. *Physics in Medicine and Biology*, 35(8), 1119–1128.
- Truong, D. Q., Huber, M., Xie, X., Datta, A., Rahman, A., Parra, L. C., ... Bikson, M. (2014). Clinician accessible tools for GUI computational models of transcranial electrical stimulation: BONSAI and SPHERES. *Brain Stimulation*, 7(4), 521–524.
- Truong, D. Q., Magerowski, G., Blackburn, G. L., Bikson, M., & Alonso-Alonso, M. (2013). Computational modeling of transcranial direct current stimulation (tDCS) in obesity: Impact of head fat and dose guidelines. *NeuroImage Clinical*, 2, 759–766.
- Turkeltaub, P. E., Benson, J., Hamilton, R. H., Datta, A., Bikson, M., & Coslett, H. B. (2012). Left lateralizing transcranial direct current stimulation improves reading efficiency. *Brain Stimulation*, 5(3), 201–207.
- Wagner, T., Eden, U., Rushmore, J., Russo, C. J., Dipietro, L., Fregni, F., ... Valero-Cabré, A. (2014a). Impact of brain tissue filtering on neurostimulation fields: A modeling study. *NeuroImage*, 85(Pt 3), 1048–1057.
- Wagner, T., Fregni, F., Fecteau, S., Grodzinsky, A., Zahn, M., & Pascual-Leone, A. (2007). Transcranial direct current stimulation: A computer-based human model study. *NeuroImage*, 35(3), 1113–1124.

- Wagner, S., Rampersad, S. M., Aydin, U., Vorwerk, J., Oostendorp, T. F., Neuling, T., ... Wolters, C. H. (2014b). Investigation of tDCS volume conduction effects in a highly realistic head model. *Journal of Neural Engineering*, *11*(1), 016002.
- Wiethoff, S., Hamada, M., & Rothwell, J. C. (2014). Variability in response to transcranial direct current stimulation of the motor cortex. *Brain Stimulation*, *7*(3), 468–475.
- Windhoff, M., Opitz, A., & Thielscher, A. (2013). Electric field calculations in brain stimulation based on finite elements: An optimized processing pipeline for the generation and usage of accurate individual head models. *Human Brain Mapping*, *34*(4), 923–935.
- Woods, A. J., Antal, A., Bikson, M., Boggio, P. S., Brunoni, A. R., Celnik, P., ... Nitsche, M. A. (2016). A technical guide to tDCS, and related non-invasive brain stimulation tools. *Clinical Neurophysiology*, *127*(2), 1031–1048.